

Contact enhancement of locomotion in spreading cell colonies

Joseph d'Alessandro^{*†‡}, Alexandre Solon[§], Yoshinori Hayakawa,[¶] Christophe Anjard,[†] François Detcheverry,[†] Jean-Paul Rieu[†] and Charlotte Rivière^{*†}

The dispersal of cells from an initially constrained location is a crucial aspect of many physiological phenomena ranging from morphogenesis to tumour spreading. In such processes, the way cell-cell interactions impact the motion of single cells, and in turn the collective dynamics, remains unclear. Here, the spreading of micro-patterned colonies of non-cohesive cells is fully characterized from the complete set of individual trajectories. It shows that contact interactions, chemically mediated interactions and cell proliferation each dominates the dispersal process on different time scales. From data analysis and simulation of an active particle model, we demonstrate that contact interactions act to speed up the early population spreading by promoting individual cells to a state of higher persistence, which constitutes an as-yet unreported contact *enhancement* of locomotion. Our findings suggest that the current modeling paradigm of memoryless interacting active particles may need to be extended to account for the possibility of internal states and history-dependent behaviour of motile cells.

Understanding how cell assemblies regulate their motility is a major challenge of current biophysics.¹ Indeed, collective effects in the motion of cells play a crucial role *in vivo* in processes such as wound healing², tumour progression³ or morphogenesis⁴. In understanding the often intricate relationship between the behaviours at the cellular level and the population scale, two basic questions arise: how do cell-cell interactions alter the properties of individual cell motion? How do they impact the population dynamics?

The trajectory of a cell crawling on a surface is akin to a correlated random walk characterized by a persistence time beyond which the motion becomes diffusive^{5,6}. In the absence of interactions, this would lead on long time to simple diffusion dynamics at the colony level, as captured

in descriptions based on the Fisher-Kolmogorov-Petrovski-Piskunov (FKPP) equation^{7,8}. However, the assumption of non-interacting cells is often unwarranted^{9,10}, as several types of cell-cell interactions affecting the collective dynamics have been uncovered experimentally. A first class involves long-range interactions, which may be mediated by a chemical^{11,12} as in quorum sensing, or by the substrate¹³. A second class includes short-range contact interactions: volume exclusion, cell-cell adhesion or contact inhibition of locomotion (CIL)¹⁴, which acts to change the direction of motion of a cell upon contact with another cell.

Despite their local nature, contact interactions have proven essential to the collective behaviour of cells, at least for dense assemblies with density near close-packing. On the edge of a dense colony, CIL¹⁵ or excluded volume¹⁶ combined with a density gradient acts to bias the motion towards free space^{10,17,18}, hence facilitating the spreading of the colony^{9,16,19}. This effect is further reinforced by the tension created by leader cells through adherens junctions^{17,20}. In the bulk of a tissue, force transmission through adherens junctions^{21,22} (but also nematic alignment^{23,24} or simple volume exclusion²⁵) can lead to coordinated motion over several cell sizes and induce active jamming and glassy behaviour^{26,27,28}. The slowing down of tissue dy-

* <To whom correspondence should be addressed. E-mail: joseph.d'alessandro@ijm.fr, charlotte.riviere@univ-lyon1.fr>

[†]Institut Lumière Matière, CNRS UMR 5306, Université Claude Bernard Lyon 1, Université de Lyon, Lyon, 69622 Villeurbanne Cedex, France

[‡]Current address: Institut Jacques Monod (IJM), CNRS UMR 7592 et Université Paris Diderot, 75013 Paris, France

[§]Department of Physics, Massachusetts Institute of Technology, Cambridge, MA 02139, USA

[¶]Center for Information Technology in Education, Tohoku University, Sendai 980-8578, Japan

namics is especially clear in cell systems dominated by CIL¹⁵, which reduces the cell persistence²⁹ or effective speed³⁰.

Here, we investigate collective cell migration at moderate density in assemblies lacking cell-cell adhesion. In contrast to the high-density regime, this region has received comparatively much less attention so far. By studying the spreading dynamics of micropatterned *Dictyostelium discoideum* cell colonies, we find that cell-cell contacts enhance the cell persistence, an effect that we refer to as contact enhancement of locomotion (CEL). This phenomenon results in a speed-up of the colony spreading upon increasing the packing fraction and defines a novel kind of interaction, which, instead of acting instantaneously as a physical force, modifies the internal state of the moving agents and their subsequent behaviour.

A highly controlled model of cell colony

We used vegetative *Dictyostelium discoideum* (*D.d.*) cells, which are often considered as a benchmark for the amoeboid motility of fast-moving cells^{31,32,33}. Moreover, they are especially adapted to study the role of interactions in the absence of strong cell-cell adhesion, as they do not form such adhesions in nutrient-rich conditions³⁴. To experimentally mimic the dispersal of cells from an initial location in a reproducible way, we constrained a controlled number of cells in a disk of diameter 320 μm , using PDMS micro-stencils^{35,17} (Fig. 1a). Taking off the micro-stencil, we let them migrate freely outwards and image the colony for durations ranging from 8 h to 48 h (see snapshots in Fig. 1b and Supplementary Movie 1).

We characterize the colony spreading both at the population and individual cell levels (Fig. 1c). Making use of the circular symmetry, field quantities such as the density (Fig. 1c) are averaged over concentric rings and depend only on time t and the distance r from the centre of the colony. At short times, we first observe a decrease of the density in the centre of the colony as it spreads to invade free space. Then, on time scales of the order of the doubling time $\beta^{-1} \sim 9$ h, the density starts increasing uniformly because of cell divisions. Finally, after

about 40h the density saturates at a carrying capacity $\rho_{max} \approx 5 - 8 \times 10^5 \text{ cell/cm}^2$ (Fig. 1c).

The spreading of the colony is found to be faster in the first few hours of the experiment. Using the single cell trajectories obtained by automated cell tracking, this observation can be related to the average cell speed (see Supplementary Figure 1): After an initial increase, the cell speed decreases until it reaches a low-motility plateau at $t \approx 10$ h. This behaviour at long times is well explained by the overall regulation of the motility through a secreted quorum-sensing factor, which has been evidenced in our group before¹¹. Indeed, when repeating the spreading experiments with a continuous perfusion of fresh medium to rinse out secreted molecules, the decrease in motility is suppressed and the colony instead rapidly reaches a high-motility plateau (see Supplementary Figure 1a). As soon as the perfusion stops, the concentration of quorum-sensing factors builds up and the cell speed falls down.

Collective effects on the short-time spreading

We now focus on the short-time spreading of the colony. It strikingly reveals that the higher the cell density, the faster the colony spreads (Fig. 2a-b and Supplementary Movies 2-3). This collective effect is seen on the density profiles or on the gyration radius, $R_g = \sqrt{\langle r^2 \rangle}$, which quantifies the size of the colony (see Fig. 2c-e). To better characterise this effect, we compute the radial component v_r of the velocity of each cell, and average over the colony. We find that this averaged $\langle v_r \rangle$ exhibits a positive peak around 100 min in the colonies with higher initial density $N_0 = 246 \pm 66$ (Fig. 2f and Supplementary Figure 1). This implies that, in this time frame, cells move outward in average.

The existence of a non-vanishing radial velocity is not surprising in itself since it is the analogue, for self-propelled particles³⁶, of an outward diffusive flux. However, one expects the peak to be located at a time of the order of the persistence time of the particles (see Fig. 4), which is found around $\tau_p \sim 5$ min for *D.d.* cells in similar conditions^{11,37}. On the contrary, the radial velocity peak happens here on a much longer time scale ~ 100 min. It strongly suggests that

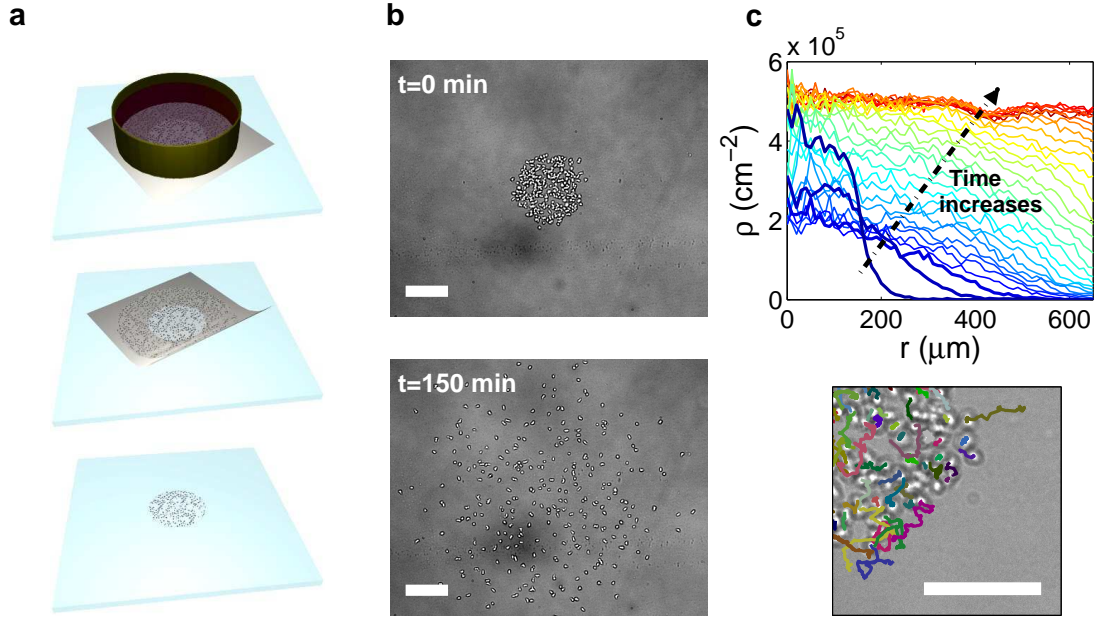


Figure 1: A highly-controlled experimental set-up gives full access to colony spreading dynamics at both individual and population scales.

(a) Cartoon of the patterning technique. The cells are first deposited in a home-made well (brown) on top of a PDMS stencil (light gray) made by soft-lithography techniques (top). After 45 min of adhesion, the well and the stencil are removed (centre), creating an initial circular pattern of 320 μm in diameter (bottom), whose spreading is then followed by time-lapse microscopy. (b) Snapshots of a colony with $N_0 = 245$ cells initially at $t = 0$ min (top) and $t = 150$ min (bottom). Scale bars: 200 μm . (c) Top: Evolution of the density profiles $\rho(r, t)$ over 60 h (from blue to red) for one colony with initially $N_0 = 349$ cells. All the curves are separated by a 2 h interval. The first three curves are drawn thicker to highlight the fast initial spreading of the colony. Bottom: Cell trajectories at the edge of the initial spot, from $t = 0$ min to $t = 60$ min. Scale bar 100 μm .

an unknown effect speeds up the spreading on this longer time scale. Importantly, this effect neither originates from cell division (it happens on a time-scale much shorter than the doubling time) nor from distant chemically-mediated interactions arising from bulk soluble molecules (see Supplementary Figure 1) or from deposited trails (see Supplementary Figure 2).

Most interestingly, we find that the amplitude of the peak in radial velocity strongly depends on the number of cells in the colony (Fig. 2f). Thus, the spreading rate is collectively increased through local interactions likely occurring when cells are in contact. To understand this density-dependent spreading dynamics, we now turn to a more refined analysis of the motion of individual cells.

Cell-cell contacts increase their persistence

From our dataset of trajectories, we find that the short-time speed-up of colony spreading is controlled by a transient increase in the persistence of the cells, the effect being more pronounced the denser the initial colony. This statement, illustrated by sample trajectories in Figure 3a-b and Supplementary Figure 4, is motivated by a body of quantitative measurements.

First, the cells appear more elongated, hence more polarised, in denser colonies (Fig. 3a). It is quantified by computing the cell contours' eccentricity, which increases with density at early times before relaxing to values corresponding to more isotropic cell shapes (see Supplementary Figure 3).

Second, we used the coefficient of movement efficiency (CME, see Methods) to estimate the per-

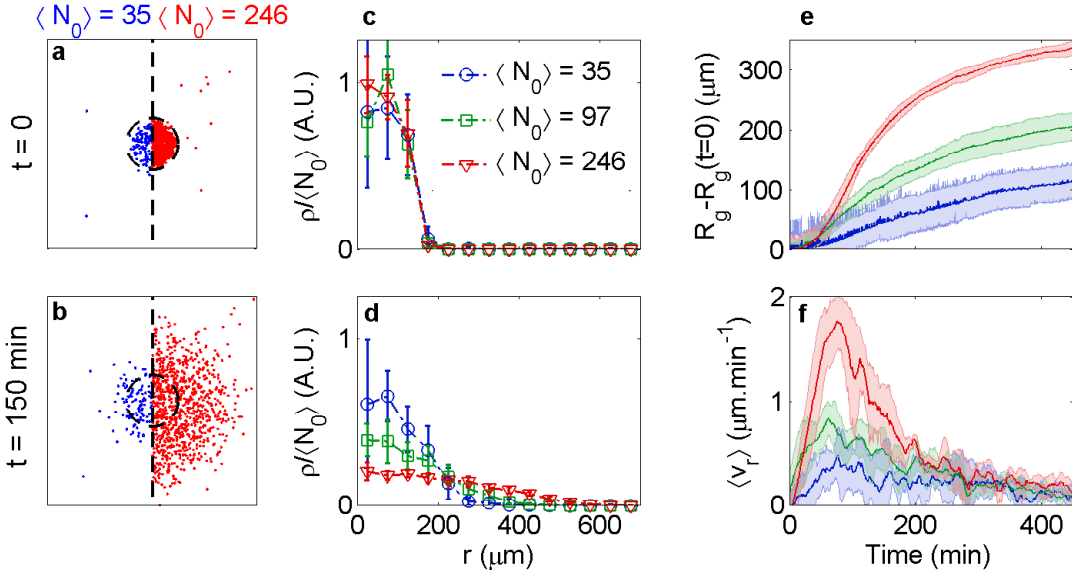


Figure 2: Density-dependent colony spreading.

The experiments are divided in three groups to study the effect of the initial cell number N_0 . (a-b) “Snapshots” of the colonies for two different groups $N_0 = 35 \pm 12$ (blue, left, 208 cells in total) and 246 ± 66 (red, right, 1229 cells in total), at $t = 0$ and $t = 150$ min. The positions of all cells in each group of experiments are represented as coloured points. The dashed circle denotes the edge of the stencil. (c-d) Normalised density profiles for each group at $t = 0$ min (c) and $t = 150$ min (d). (e) Gyration radius $R_g = \sqrt{\langle r^2 \rangle}$ of the colonies as a function of time. (f) Radial velocity $\langle v_r \rangle$ as a function of time averaged over the colony (same colour code for every panel). The error bars are the standard deviation ($n = 6, 8, 5$ experiments respectively for $N_0 = 35 \pm 12, N_0 = 97 \pm 25, N_0 = 246 \pm 66$).

sistence of the trajectories with good time and space accuracy. This quantity, for a given interrogation time Δt , ranges from 0 for a motion with persistence time much smaller than Δt to 1 for ballistic motion. From the spatio-temporal evolution of the CME measured with $\Delta t = 5$ min, it is clear that the persistence increases with density (Fig. 3c). This is especially pronounced at short times and near the periphery of the colony, where the radial velocity map also exhibits high values (Fig. 3d).

Finally, another quantitative characterisation is provided by the velocity direction autocorrelation function $C(t' - t) = \langle \mathbf{u}(t') \cdot \mathbf{u}(t) \rangle$, where \mathbf{u} is the direction of motion of a cell. The simplest models of persistent motion (Ornstein-Uhlenbeck, active Brownian particle or run-and-tumble motion) all lead to an autocorrelation function which decays exponentially over the persistence time. In contrast, our data is better described by a sum of two exponentials (Fig. 3e):

$$C(t) = c e^{-\gamma t} + c' e^{-\gamma' t}. \quad (1)$$

This form could equally arise because of two distinct populations of cells with different persis-

tence time or because of a bimodal motion of individual cells^{41,44,42}. However, the first possibility can be ruled out since the relative weights c and c' are not constant in time.

Thus, all experimental clues point to the fact that each cell is able to increase its persistence upon collision. For modeling simplicity, although we cannot rule out completely a continuous change, we consider cells that switch between two modes of motion, a mode 1 which persistence time is D_{r1}^{-1} and average duration τ_1 , and a mode 2 with $D_{r2} < D_{r1}$ and τ_2 . We used this model to fit all experimental data, as explained in the Supplementary Information, assuming for simplicity that the mode of higher persistence is ballistic ($D_{r2} = 0$). Fig. 3e shows representative examples for this fitting procedure. As an output, we obtain the estimates $D_{r1}^{-1} = 2$ min and $\tau_2 = 10$ min (see Supplementary Figure 5), and the fraction $\phi_2(t) = \tau_2 / (\tau_1 + \tau_2)$ of cells in mode 2 (Fig. 3f). Like the radial velocity, $\phi_2(t)$ reaches a maximum at around 100 min, and exhibits an overall increase with density, showing that higher densities pro-

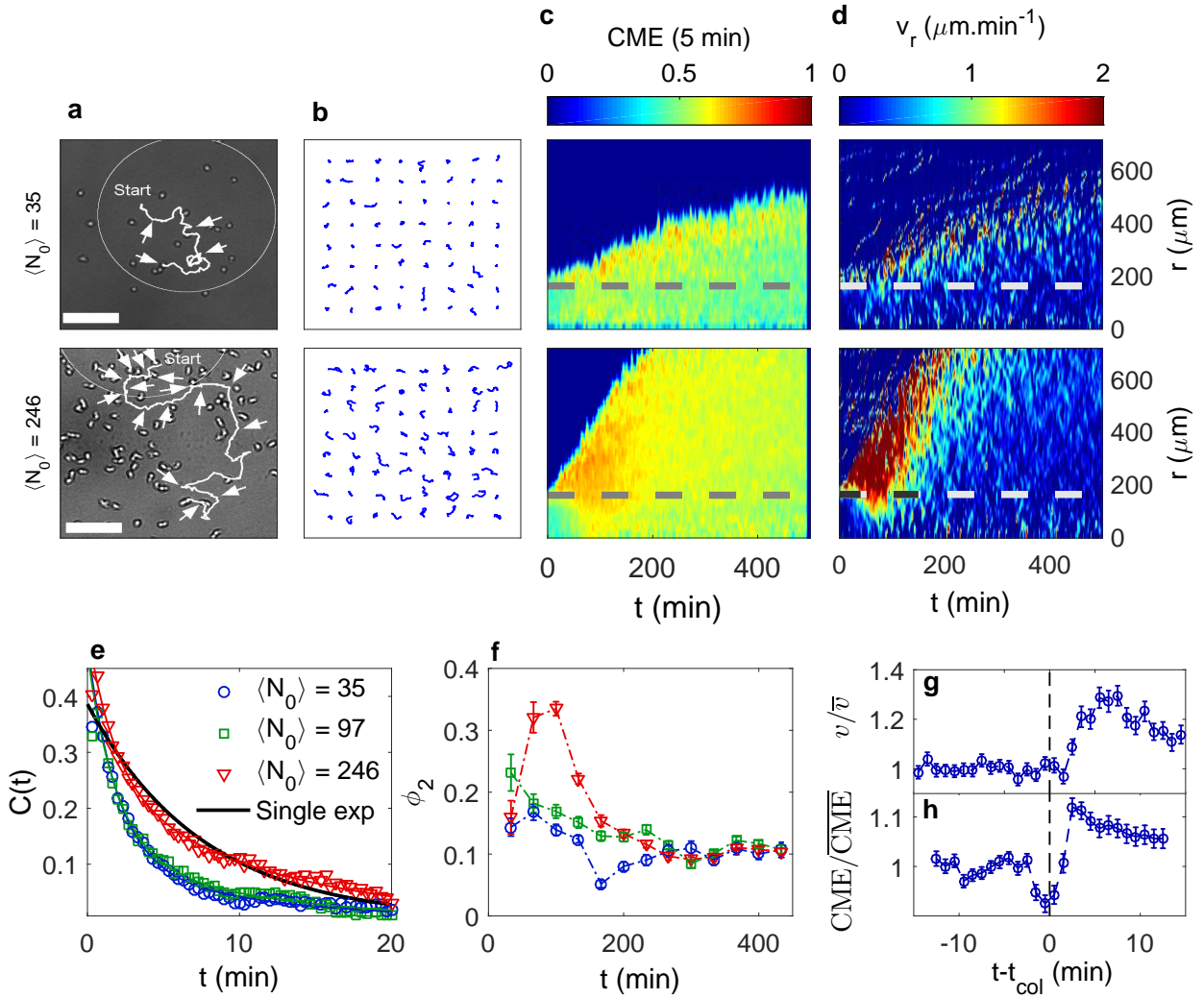


Figure 3: Local interactions between cells lead to an increase in cell persistence.

(a–d) Comparison of trajectory properties at low ($\langle N_0 \rangle = 35$, top row) and high ($\langle N_0 \rangle = 246$, bottom row) initial densities. (a) Typical cell trajectory (plotted over 100 min), with “Start” denoting the initial cell position, the white circle representing the border of the initial pattern and the arrows pointing to collision events; (b) 64 examples of trajectories from $t = 100$ min to $t = 130$ min, picked randomly over all cell trajectories; (c) spatio temporal dynamics of the CME with $\Delta t = 5$ min and (d) of the radial velocity v_r (the dashed lines represent the border of the initial colonies). (e) Velocity direction autocorrelation function at $t = 67 - 133$ min for various $\langle N_0 \rangle$ (symbols, same colour code for panels e and f) and fits using the expression detailed in Supplementary Information (solid lines) with $D_{r1}^{-1} = 2$ min and $\tau_2 = 10$ min. The thick black line represents the best single-exponential (‘Single exp’) fit for $\langle N_0 \rangle = 246$, which misses the experimental behaviour at both very short and long times. (f) Proportion ϕ_2 of cells in mode 2 as extracted from the fit of the correlation functions (the lines are guides for the eye). The error bars represent the 95% confidence interval for the fit parameter. (g–h) Normalised speed (g) and CME computed with $\Delta t = 5$ min (h) for cells undergoing a single collision at $t = t_{\text{col}}$ within a 30 min interval. \bar{v} (resp. $\overline{\text{CME}}$), denote the basal speed (resp. CME) before collision. The error bars show the SEM for the $n = 464$ pieces of trajectory from 232 collisions.

mote switching to the persistent mode.

Because this enhancement of persistence is not chemically mediated (see Supplementary Figs. 1 and 2) and depends strongly on the density (Figs. 2 and 3), we conclude that contacts –

understood here as collisions or short-range interactions – are the primary cause for the phenomenon. Paralleling the CIL acronym, hereafter we refer to this effect as CEL, or contact enhancement of locomotion. To confirm more

directly the existence of this phenomenon, we look at the statistics of cell-cell contacts. As described in the Supplementary Information, we retain only “clean” contacts (between cells undergoing no other collision for 15 min before and after). We compare the speed and CME of each single cell before and after collision and then average over all available data (see Fig. 3g–h, and Supplementary Figures 10–12). Both computed quantities exhibit a significant transient increase, demonstrating that CEL is indeed responsible for the density-dependent spreading rate of the colonies. Note that the analysis of the angular scattering (see Supplementary Figures 8–9) show that the cell-cell contacts have no aligning effect likely to promote collective motion and to increase the spreading rate by itself.

Comparison with minimal active particle models

To support our experimental findings, we now investigate several minimal active particle models. Discarding other types of contact interactions, we show that a collision-induced increase in persistence is necessary and sufficient to account for the salient features of the short-time dynamics of the colony spreading.

Let us consider self-propelled hard disks moving at a constant velocity v . In addition, the direction of motion θ of a particle is subject to rotational diffusion with coefficient D_r . The motion of the i^{th} particle is thus governed by the following equations

$$\partial_t \mathbf{r}_i = v \mathbf{u}(\theta_i) + \sum_{j \neq i} \mathbf{f}_{ij}(\mathbf{r}_i - \mathbf{r}_j) \quad (2)$$

$$\partial_t \theta_i = \sqrt{2D_r} \eta_i(t), \quad (3)$$

where $\mathbf{u}(\theta_i) = (\cos \theta_i, \sin \theta_i)$ and η_i is a delta-correlated Gaussian white noise with zero mean and unit variance. \mathbf{f}_{ij} is the steric repelling force exerted by particle j on particle i (see Methods for more details). As such, Eqs. (2–3) describe the active Brownian particle (ABP) model, well-studied as a minimal model of phase-separating active particles^{30,38}, and a suitable basis for the modelling of the persistent random motion of cells. Consistently with the experiments, we take $v = 5 \mu\text{m} \cdot \text{min}^{-1}$ and initially place the particles in a disk of $320 \mu\text{m}$ in diameter. The resulting average radial velocity and radius of gy-

ration measured in the simulations are shown as a function of time in Fig. 4.

First, we checked whether this simple interaction rule could yield a density-dependent spreading. Indeed, if we think of moving cells as hard-core spheres undergoing a persistent random walk, the excluded-volume (EV) between the cells gives rise to an outward pressure³⁸. This effect is also present for Brownian hard spheres, for which it can be taken into account by an effective diffusion coefficient increasing with concentration³⁹. However, in the present experiments where cells are relatively sparse – with packing fractions up to 0.3 – this pressure is not expected to play an important role and indeed, simulations of Eqs. (2)–(3) with only hard-core repulsion exhibit no effect of density (Fig. 4, left).

We then further implemented the effect of CIL that is, upon collision, cells actively reorient away from the contact. To that end, we added an angular repulsion to the equations of motion, in the form of a torque acting on cells undergoing a contact: $\Gamma \sum_{j \neq i} H(\|\mathbf{r}_j - \mathbf{r}_i\| - \sigma_r) \sin(\theta_i - \beta_{ij})$ in equation (3), where $\beta_{ij} = \arg(\mathbf{r}_j - \mathbf{r}_i)$, H is the Heaviside step function implementing the finite radius of interaction and σ_r is the contact distance (see Methods). Qualitatively, one can imagine that by reorienting the direction of motion of particles toward free space, active reorientation could explain the experimental data¹⁵. However, even with a large value $\Gamma = 100 \text{ min}^{-1}$ corresponding to quasi-instantaneous reorientation, the density-dependent increase in average radial velocity and spreading rate is an order of magnitude smaller than in the experiment (Fig. 4, centre). In addition, the (very limited) peak in radial velocity appears at a very early time, at odds with the experimental observation. In both situations, the rotational diffusion was set to $D_r^{-1} = 5 \text{ min}$ to match the average persistence time of experimental trajectories.

Finally, guided by the experimental observations, we tested a minimal model of CEL: After each contact, two particles involved in a collision enter a mode of high persistence (Fig. 4, right). For simplicity, the speed is kept constant and the motion is taken to be ballistic in this high persistence (mode 2) state. The particles then relax to the basal (mode 1) state at a rate $\lambda_2 = \tau_2^{-1}$. We fix $D_{r1}^{-1} = 2 \text{ min}$ and $\tau_2 = 10 \text{ min}$, as determined from the fit of the experimental data (see

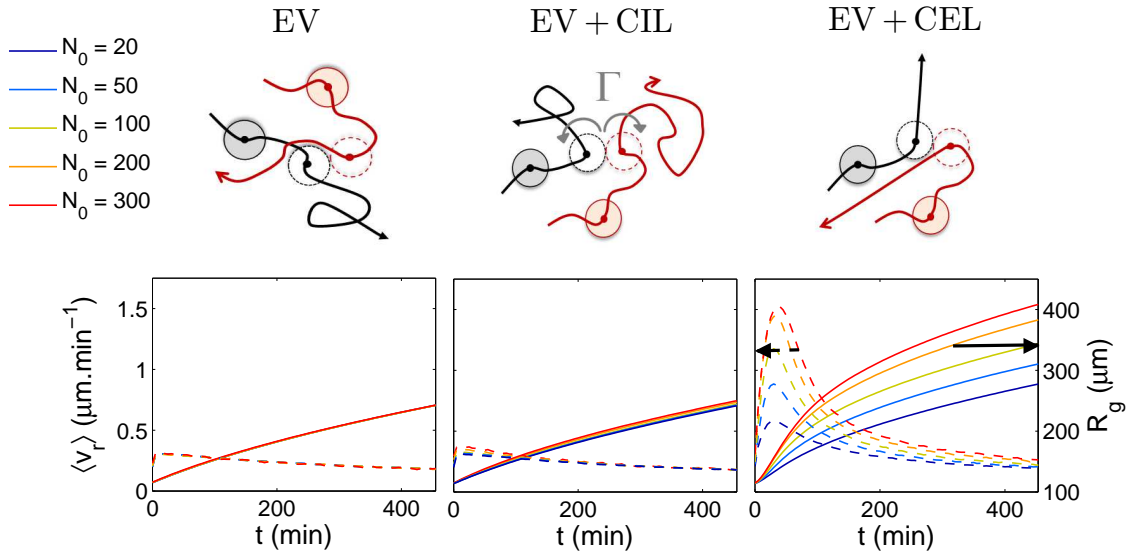


Figure 4: Spreading colonies in a particle-based model mimicking the experiments. Radial velocity $\langle v_r \rangle$ (dashed lines, left axes) and colony radius R_g (solid lines, right axes) in simulated colonies with different numbers of particles N_0 in the three models considered. The cartoons on the top row illustrate the different contact rules: Excluded-volume only (EV, left), excluded-volume and angular repulsion (EV + CIL, center), excluded-volume and contact enhancement of locomotion (EV + CEL, right).

Fig. 3). The proportion ϕ_2 of cells in the persistent mode (shown in Supplementary Figure 6a) evolves with time in a density-dependent manner due to changes in the collision frequency.

We find that this model captures well the collective spreading of the colony. Indeed, as shown in Fig. 4, the amplitude and density-dependence of the peak in radial velocity, as well as the faster increase of R_g at higher density, are well captured. Overall, given the simplicity of the model, the agreement between simulations and experiments appears surprisingly good (see Supplementary Movies 2–5 for a visual comparison).

Discussion

We studied the dynamics of spreading colonies of *D.d.* cells. Using a micro-fabrication technique, we were able to produce initial colonies with controlled shape and number of cells. We showed that the long-time dynamics of the spreading is controlled by cell divisions and long-range interactions through a quorum-sensing factor. On the contrary, these two effects are absent from the short-time dynamics, thus allowing us to study the effect of cell-cell contacts. We found that cell contacts enhance the spreading of the

colony by increasing the speed and the persistence time of the cells motion. This *contact enhancement of locomotion* is further supported by a simple active particle model reproducing the main characteristics of the experimental data.

The phenomenon of “CEL” that we have described here seems *a priori* different from CIL, which acts to change the direction of motion of colliding cells. However, they are not mutually exclusive (see Supplementary Figure 12) and could even share a common microscopic origin. Indeed, the current explanation for CIL is that the protrusions driving the motion are inhibited in the contact region^{15,45}. Other protrusions can thus develop elsewhere on the cell’s periphery, leading to a new direction of motion. We could hypothesize that, similarly, either the inhibition of ruffling in the contact region or the stabilisation of the new protrusions reinforces the new polarity thereby increasing the speed and persistence of the motion. An important difference between the two effects is that CEL involves memory while CIL is usually modeled as an “instantaneous” contact process^{46,47,48,49}. The two could have different relative importances depending on the situation. For example, in dense cell clusters, the reorientation induced by CIL forces the particles on the

edge to move outward^{4,47} whereas, as we saw, in sparser colonies the increase in persistence is the dominating effect.

The importance of contact interactions *in vivo* is not completely understood. CIL has been found to play an important role in neural crest migration⁴ and the loss of heterotypic CIL (between different cell types) is thought to be crucial in the invasion of healthy tissues by cancer cells^{3,50}. Similarly, CEL could be an advantage in invading the surrounding environment efficiently, in the case of a less cohesive group of cells. Such a situation can be encountered during the escape of highly metastatic and invasive cancer cells, as well as in cell morphogenesis and microbial dispersal. More generally, it should be noticed that CEL is reminiscent of escape mechanisms, found in various organisms, which involve a temporary change of the motile behaviour and can lead to surprising collective effects⁵¹.

Finally, the new type of interaction uncovered here opens questions for active matter. Indeed, it exemplifies the wide range of possible interactions between active particles, compared to the usual “physicist’s particles”, which can lead to a rich phenomenology. It opens the door to further studies of interactions that act on an additional internal degree of freedom, which could exhibit other interesting effects.

METHODS

Cell culture

We used *Dictyostelium discoideum* cells from the strain AX2. The cells were cultured on cell-culture-treated Petri dishes (BD Falcon) in HL5 medium with glucose (Formedium) and kept in a temperature-controlled incubator at 22.5°C, with a doubling time $\beta^{-1} \sim 9$ h. Before every experiment, the cells were detached from the dish, centrifuged 5 min at 663g, harvested and resuspended at the seeding density.

Sample preparation

A reusable mould on Si wafer comprising an array of squares with circular pillars of height ~ 150 μm and diameter 320 μm in the centre was fabricated in SU8 photoresist using classical soft lithography techniques and its surface was silanized to make it non-adherent. PolyDiMethylsulfoxide (PDMS, Corning) mixed with curing agent at a 1:10 mass ratio was spin

coated on the mould for 1 min at 750 rpm to a target thickness of 70 μm . The squares were cut and peeled off. Usually a thin PDMS membrane obstructed the hole. It was then removed with a surgical blade under the microscope at low magnification.

The square stencil was stuck on the ground of a 3.5 cm wide culture dish and a homemade small plastic well was stuck on it using silicon seal. A droplet of medium was deposited into the well and the sample was placed under vacuum for 15 min to help the medium enter the central hole of the stencil and wet the dish’s surface.

The cell suspension was added in the well and the sample was placed in the incubator for 45 min to let the cells sediment and adhere. Then, the plastic well and the stencil were removed with surgical tweezers. Last, the spreading colony was imaged using a slightly defocused bright-field microscope (TE2000, Nikon) at 10X magnification and a wide-field Andor Zyla sCMOS camera. A time-lapse movie was recorded for up to 48 h using MicroManager software with a 20 s time-interval, while the temperature was kept constant at 22.5°C.

For perfusion experiments, we designed a macrofluidic chamber by sealing the culture dish with an adapted cover containing an input and an output tube. The former was linked to a 1 L supply bottle of fresh HL5 medium under controlled overpressure (OB1 controller, Elveflow) while the latter was linked to a disposal bottle. All the system was closed sterilely. We used a flow rate of 100 mL/h so that the chamber volume of about 10 mL was completely renewed every 6 minutes. We were thus able to maintain a stable medium renewal over 9 hours.

Image processing

The cells’ positions were retrieved using homemade ImageJ macros based on the ‘Find Maxima’ built-in function. Then the individual trajectories were reconstructed with a squared-displacement minimization algorithm (<http://site.physics.georgetown.edu/matlab/>) and the data analysed using homemade Matlab programs.

In particular, the CME was defined as:

$$\text{CME}_{\delta t}(t) = \frac{\|\mathbf{r}(t + \frac{\delta t}{2}) - \mathbf{r}(t - \frac{\delta t}{2})\|}{\int_{t' = t - \frac{\delta t}{2}}^{t + \frac{\delta t}{2}} \|\mathbf{v}(t')\| dt'} \quad (4)$$

Simulations

Simulations were carried out by integrating the Langevin equations Eqs. (2-3) using a Euler integration scheme with time steps $\Delta t = 10^{-3}$ min. The

hard-core repulsion between particles is modelled by a Weeks-Chandler-Andersen potential $V(r) = 4 \left[\left(\frac{\sigma}{r}\right)^{12} - \left(\frac{\sigma}{r}\right)^6 \right] + 1$ if $r < 2^{1/6}\sigma$ and 0 otherwise, where $\sigma = 10 \mu\text{m}$ is the particle diameter. We define two particles as being in contact when their relative distance $r < \sigma_r = 2^{1/6}\sigma$. In the simulations with CIL, the torque term is turned on only during the contacts, when $r < \sigma_r$. In the simulation including CEL, a contact triggers a ballistic run which lasts for an exponentially distributed time with rate λ_2 .

References

- [1] Travis, J. Mysteries of the cell: Cell biology's open cases. *Science* **334**, 1051 (2011).
- [2] Friedl, P. & Gilmour, D. Collective cell migration in morphogenesis, regeneration and cancer. *Nat Rev Mol Cell Biol* **10**, 445–457 (2009).
- [3] Friedl, P. & Wolf, K. Tumour-cell invasion and migration: diversity and escape mechanisms. *Nature Reviews Cancer* **3**, 362–374 (2003).
- [4] Carmona-Fontaine, C. *et al.* Contact inhibition of locomotion in vivo controls neural crest directional migration. *Nature* **456**, 7224 (2008).
- [5] Selmeçzi, D. *et al.* Cell motility as random motion: A review. *European Physical Journal: Special Topics* **157**, 1–15 (2008).
- [6] Li, L., Norrelkke, S.F. & Cox, E.C. Persistent cell motion in the absence of external signals: A search strategy for eukaryotic cells. *PLoS ONE*, **3**, 5 (2008).
- [7] Kolmogorov, A., Petrovskii, I. & Piscounov, N. A study of the diffusion equation with increase in the amount of substance, and its application to a biological problem. *Math. Mech.* **1**, 1–25 (1937).
- [8] Simpson, M.J. *et al.* Quantifying the roles of cell motility and cell proliferation in a circular barrier assay. *Journal of the Royal Society, Interface / the Royal Society* **10**, 20130007 (2013).
- [9] Sengers, B.G., Please C.P. & Oreffo R.O.C. Experimental characterization and computational modelling of two-dimensional cell spreading for skeletal regeneration. *Journal of the Royal Society, Interface / the Royal Society*, **4**, 1107–1117 (2007).
- [10] Marel, A.K. *et al.* Flow and Diffusion in Channel-Guided Cell Migration. *Biophys. J.*, **107**, 1054–1064 (2014).
- [11] Golé, L., Rivière, C., Hayakawa, Y. & Rieu, J.P. A quorum-sensing factor in vegetative Dictyostelium Discoideum cells revealed by quantitative migration analysis. *PLoS ONE* **6**, 1–9 (2011).
- [12] Phillips, J. & Gomer, R. A secreted protein is an endogenous chemorepellant in *Dictyostelium discoideum*. *Proc. Natl Acad. Sci. USA*, **109**, 10990–10995 (2012).
- [13] Angelini, T.E., Hannezo, E., Trepap, X., Fredberg, J.J. & Weitz, D.A. Cell migration driven by cooperative substrate deformation patterns. *Phys. Rev. Lett.* **104**, 168104 (2010).
- [14] Abercrombie, M. & Heaysman, J.E. Observations on the social behaviour of cells in tissue culture: I. Speed of movement of chick heart fibroblasts in relation to their mutual contacts. *Experimental cell research* **5**, 111–131 (1953).
- [15] Mayor, R. & Carmona-Fontaine, C. Keeping in touch with contact inhibition of locomotion. *Trends in cell biology* **20**, 319–328 (2010).
- [16] Dyson, L. & Baker, R.E. The importance of volume exclusion in modelling cellular migration. *J. Math. Biol.* **71**, 679–711 (2014).
- [17] Serra-Picamal, X. *et al.* Mechanical waves during tissue expansion. *Nat. Phys.* **8**, 628–634 (2012).
- [18] Nnetu, K.D., Knorr, M., Strehe, D., Zink, M. & Käs, J.A. Directed persistent motion maintains sheet integrity during multicellular spreading and migration. *Soft Matter* **8**, 6913 (2012).
- [19] Yates, C.A., Parker, A. & Baker, R.E. Incorporating pushing in exclusion-process models of cell migration. *Phys. Rev. E* **91**, 052711 (2015).
- [20] Sepúlveda, N. *et al.* Collective cell motion in an epithelial sheet can be quantitatively

- described by a stochastic interacting particle model. *PLoS Comput. Biol.* **9**, e1002944 (2013).
- [21] Petitjean, L. *et al.* Velocity fields in a collectively migrating epithelium. *Biophysical J.* **98**, 1790–1800 (2010).
- [22] Tambe, D.T. *et al.* Collective cell guidance by cooperative intercellular forces. *Nat. Mat.* **10** 469–475 (2011).
- [23] Coburn, L., Cerone, L., Torney, C., Couzin, I.D. & Neufeld, Z. Interactions lead to coherent motion and enhanced chemotaxis of migrating Cells. *Phys. Biol.* **10**, 046002 (2013).
- [24] Duclos, G., Garcia, S., Yevick, H.G. & Silberzan, P. Perfect nematic order in confined monolayers of spindle-shaped cells. *Soft Matter* **10**, 2346 (2014).
- [25] Londono C. *et al.* Nonautonomous contact guidance signaling during collective cell migration. *Proc. Natl Acad. Sci. USA* **111** 1807–1812 (2014).
- [26] Angelini, T.E. *et al.* Glass-like dynamics of collective cell migration. *Proc. Natl Acad. Sci. USA* **108**, 4714–4719 (2011).
- [27] Park, J.-A. *et al.* Unjamming and cell shape in the asthmatic airway epithelium. *Nat. Mat.* **14**, 1040–1049 (2015).
- [28] Garcia, S. *et al.* Physics of active jamming during collective cellular motion in a monolayer. *Proc. Natl Acad. Sci. USA* **112**, 15314–15319 (2015).
- [29] Vedel, S., Tay, S., Johnston, D.M., Bruus, H. & Quake, S.R. Migration of Cells in a Social Context. *Proc. Natl Acad. Sci. USA* **110**, 129–134 (2013).
- [30] Fily, Y. & Marchetti, M.C. Athermal Phase Separation of Self-Propelled Particles with No Alignment. *Phys. Rev. Lett.* **108**, 235702 (2012).
- [31] Friedl, P., Borgmann, S. & Bröcker, E. B. Amoeboid leukocyte crawling through extracellular matrix: lessons from the Dictyostelium paradigm of cell movement. *Journal of Leukocyte Biology* **70**, 491–509 (2001).
- [32] Friedl, P. & Wolf, K. Plasticity of cell migration: a multiscale tuning model. *J. Cell Biol.* **188**, 11–9 (2010).
- [33] Levine, H. Learning Physics of Living Systems from *Dictyostelium*. *Phys. Biol.* **11**, 053011 (2014).
- [34] Coates, J. C. & Harwood, A. J. Cell-cell adhesion and signal transduction during *Dictyostelium development*. *J. Cell Sci.* **114**, 4349–4358 (2001).
- [35] Poujade, M. *et al.* Collective migration of an epithelial monolayer in response to a model wound. *Proc. Natl Acad. Sci. USA* **104**, 15988–15993 (2007).
- [36] Cates, M.E. & Tailleur, J. When are active Brownian particles and run-and-tumble particles equivalent? Consequences for Motility-induced Phase Separation. *Europhys. Lett.* **101**, 20010 (2013).
- [37] Bosgraaf, L. & Van Haastert, P.J.M. The ordered extension of pseudopodia by amoeboid Cells in the absence of external cues. *PLoS ONE* **4**, 4 (2009).
- [38] Solon, A.P. *et al.* Pressure and phase equilibria in interacting active Brownian spheres. *Phys. Rev. Lett.* **114**, 198301 (2015).
- [39] Bruna, M. & Chapman, S.J. Excluded-volume effects in the diffusion of hard spheres. *Physical Review E* **85**, 011103 (2012).
- [40] Peruani, F. & Morelli, L.G. Self-propelled particles with fluctuating speed and direction of motion in two dimensions. *Phys. Rev. Lett.* **99**, 010602 (2007).
- [41] Potdar, A.A., Jeon, J., Weaver, A.M., Quaranta, V. & Cummings, P.T. Human mammary epithelial cells exhibit a bimodal correlated random walk pattern. *PLoS ONE* **5**, e9636 (2010).
- [42] Metzner, C. *et al.* Superstatistical analysis and modelling of heterogeneous random walks. *Nat. Commun.* **6**, 7516 (2015).
- [43] Selmecki, D. *et al.* Cell motility as persistent random motion: theories from experiments. *Biophys. J.* **89**, 912–931 (2005).

- [44] Maiuri, P. *et al.* Actin Flows Mediate a Universal Coupling between Cell Speed and Cell Persistence. *Cell* **161**, 374–386 (2015).
- [45] Stramer, B.A. & Mayor, R. Mechanisms and in vivo functions of contact inhibition of locomotion. *Nat. Rev. Mol. Cell. Biol.* **118** (2016).
- [46] Davis, J.R., *et al.* Emergence of embryonic pattern through contact inhibition of locomotion. *Development* **139**, 4555–4560 (2012)
- [47] Zimmermann, J., Camley, B.A., Rappel, W.-J. & Levine, H. Contact inhibition of locomotion determines cell-cell and cell-substrate forces in tissues. *Proc. Natl Acad. Sci. USA* **113**, 2660–2665 (2016).
- [48] Camley, B.A., Zimmermann, J., Levine, H. & Rappel, W.-J. Emergent collective chemotaxis without single-cell gradient sensing. *Phys. Rev. Lett.* **116**, 098101 (2016).
- [49] Szabo, A., *et al.* In vivo confinement promotes collective migration of neural crest cells. *J. Cell. Biol.* **213**, 543–555 (2016).
- [50] Abercrombie, M. Contact inhibition and malignancy. *Nature* **281**, 259–262 (1979).
- [51] Ramdya, P. *et al.* Mechanosensory interactions drive collective behaviour in *Drosophila*. *Nature* **519**, 233–236 (2015).
- [52] Heid, P. J. *et al.* The role of myosin heavy chain phosphorylation in Dictyostelium motility, chemotaxis and F-actin localization. *J. Cell Sci.* **117**, 4819–4835 (2004).

ACKNOWLEDGEMENTS

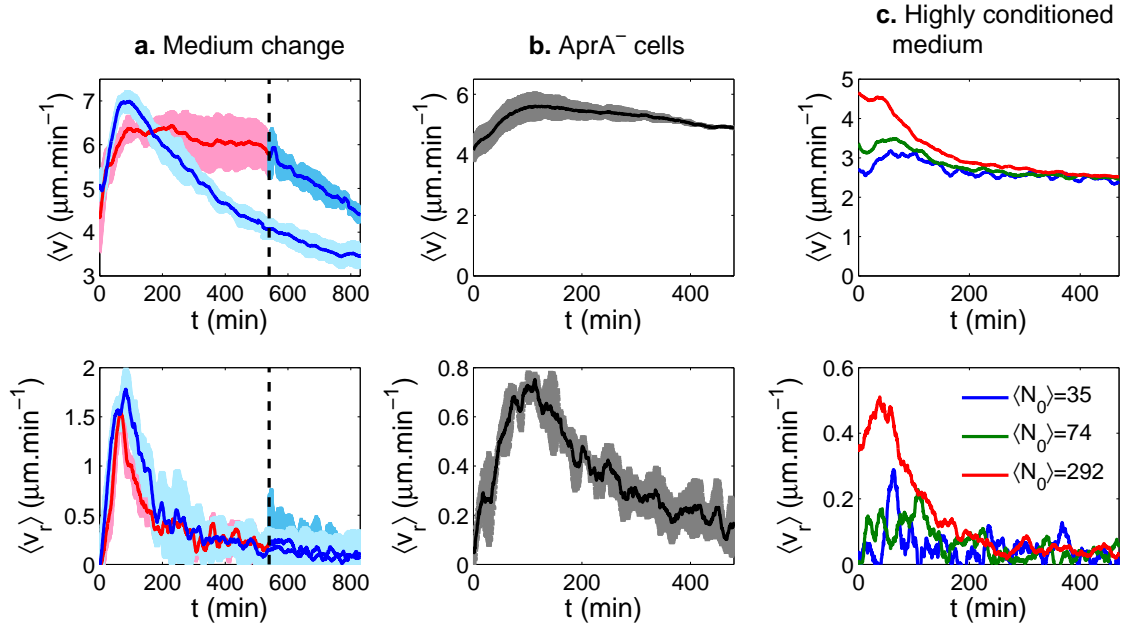
The authors are grateful to R. Fulcrand for his help in micro-fabrication, to V. Hakim for stimulating discussions and to C. Cottin-Bizonne for her comments on the manuscript. J.d.A. has been partially supported by the Fondation ARC pour la Recherche sur le Cancer and by the Programme d’Avenir Lyon-Saint Étienne. A.S. acknowledges funding through a PLS fellowship of the Gordon and Betty Moore foundation. J.d.A., C.R. and J.P.R. belong to the CNRS consortium CellTiss and to the LIA ELyT Lab.

AUTHOR CONTRIBUTIONS

J.d.A., J.P.R. and C.R. designed experiments; J.d.A. performed experiments and analysed experimental data; J.d.A. and A.S. conceived the particle-based models; A.S. performed simulations and analysed simulation data; C.A. contributed to design of experiments in Supplementary Figure 1 and provided AprA⁻ cells; F.D. computed the analytical results on bimodal trajectories and helped with the fitting procedure; Y.H. assisted in the data analysis and interpretation; J.d.A. and A.S. wrote the manuscript; F.D., J.P.R. and C.R. made substantial contribution to the manuscript; all authors discussed and interpreted the data, read and commented on the manuscript; J.P.R. and C.R. supervised the project.

Supplementary information

1 An effect of local interactions



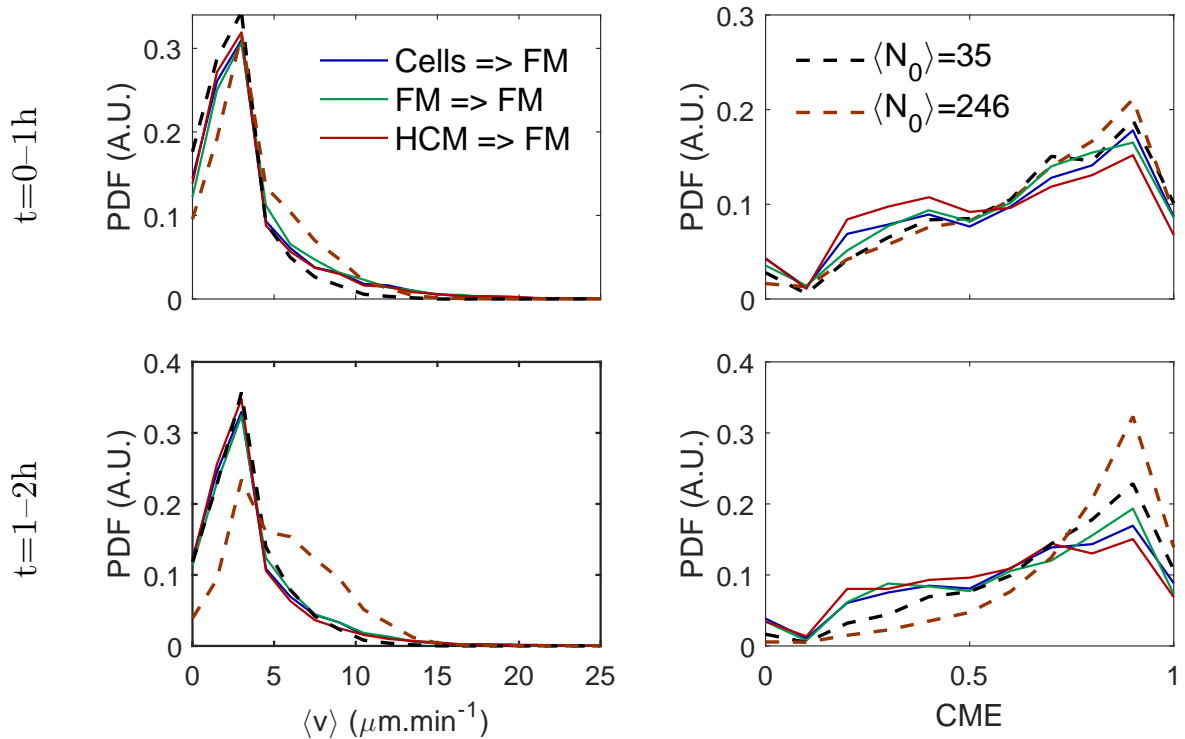
Supplementary Figure 1: The cells' outward motion is not due to a large-scale chemical communication.

Colony-averaged speed (top row) and radial velocity (bottom row) in various conditions. (a) Medium exchange. Control (blue) and samples with continuous medium exchange (red). The speed is maintained constant until the exchange is stopped (vertical dashed line), whereas the radial motion $\langle v_r \rangle$ is robust to medium exchange. (b) aprA^- cells still exhibit outward motion, although they do not secrete AprA, the only known endogenous chemorepellent in *Dictyostelium discoideum* (c) Cells in highly conditioned medium (HCM), prepared by letting cells in culture in it before filtering, so that all secreted molecules are already at a high concentration. The cell motion is affected but there is still a density-dependent peak in $\langle v_r \rangle(t)$.

We checked that long-distance interactions were not responsible for the enhancement of the colony spreading rate. To that end, we measured the average speed $\langle v \rangle$ and radial velocity $\langle v_r \rangle$ during the spreading of cell colonies in three different control conditions, as described below. We looked especially at the presence of the peak in $\langle v_r \rangle(t)$, which, in our experiments, is the macroscopic signature of the collective enhancement of the spreading. Firstly, we designed a fluidic system that allowed to continuously change the sample's medium, so that any secreted (or depleted) molecule was rinsed out (or rescued), hence preventing any large-scale chemical sensing such as chemorepulsion or quorum-sensing. It efficiently suppressed the overall regulation of cell motility through a known quorum-sensing factor (QSF)¹¹ (Supplementary Figure 1a, top), but did not affect the outward motion (Supplementary Figure 1a, bottom) which shows that the collective effect is still present. Secondly, we used aprA^- cells which do not produce the protein AprA, so far the only endogenous chemorepellent molecule known for *Dictyostelium discoideum*¹². Although the motility of these cells is slightly different from the wild-type cells, resulting in slightly modified colony dynamics, the main effect of outward motion was still observed (Supplementary Figure 1b). Last, experiments were done in highly conditioned medium (HCM). This medium is prepared by letting cells in culture in fresh HL5 medium for typically 2 days, so that it is supplemented with molecules secreted by the cells, at high concentration. Thus, one would expect the concentrations in slowly degraded molecules to be above the saturation of their detection by the cells, hence screening any additional secretion

during the experiment. Although the dynamics is again modified mainly due to the presence of QSF at high concentration in HCM¹¹, the collective effect of outward motion is still apparent in this situation (Supplementary Figure 1c).

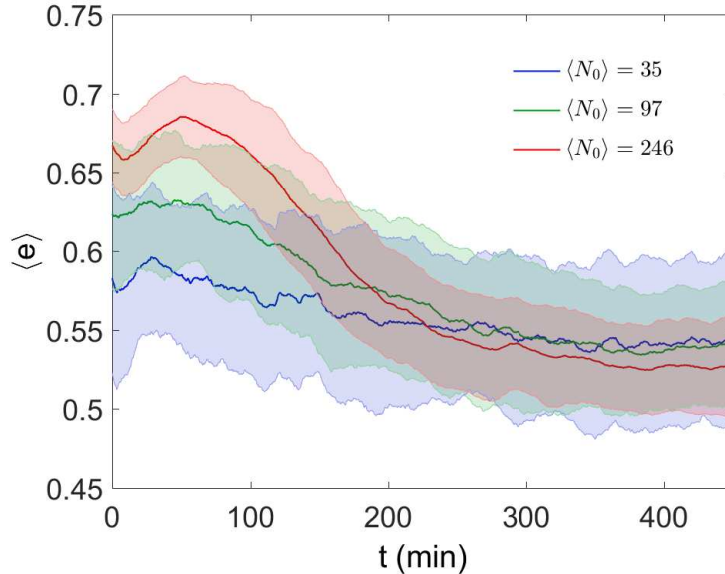
We also tested the hypothesis of cell-cell communication through the deposition of chemicals on the surface as follows. First, the sample dishes were treated by letting cells adhere on their entire surface at high density for 45 min. Then the cell layer was washed out and fresh cells were added at a low, homogeneous density with fresh medium for imaging and the single cells were tracked after 45 min adhesion. The controls include prior incubation with FM or HCM but no cell layer. If cell-cell communication through deposited trails on the surface affects the motility, there should be measurable differences between those conditions. Conversely, since the system is homogeneous and isotropic and the cells undergo almost no cell-cell contact, no effect of geometry or interaction is expected to interfere with those prior treatments. Yet, the probability density functions (PDFs) of speed and CME in the three conditions are well overlaid, showing no effect of a putative chemical deposition mechanism. Those PDFs compare very well with those measured in the low density colonies, while they differ from the high density colonies, especially around the peak of $\langle v_r \rangle(t)$ at $t = 1-2$ h (Supp. Fig. 2).



Supplementary Figure 2: Modifications of the surface by the cells do not affect cell motility. Distribution of speed (left) and CME with $\Delta t = 5$ min (right) computed from trajectories with $\delta t = 1$ min, gathered for all times $t = 0 - 1$ h (top) and $t = 1 - 2$ h (bottom) with various surface treatments (solid lines) or in spreading colonies (dashed lines). Cells \Rightarrow FM: cells were seeded at high density, let adhere for 45 min and washed out before adding fresh cells in fresh medium (FM) for imaging. FM \Rightarrow FM: the sample dish was filled with FM for 45 min before cells and FM were added for imaging. HCM \Rightarrow FM: the sample dish was filled with HCM for 45 min before cells and FM were added for imaging.

Taken together, these results show that a large-scale communication using secreted or deposited molecules is very unlikely to be at the origin of the density-dependent spreading at short times. In consequence, the interactions behind this effect must be local, whether mediated by actual cell-cell contacts or by rapidly degraded, locally accumulated chemicals. Although the latter is not inconceivable, it is less likely at stake and can be described as an “effective contact” interaction.

2 Increase in single cell persistence

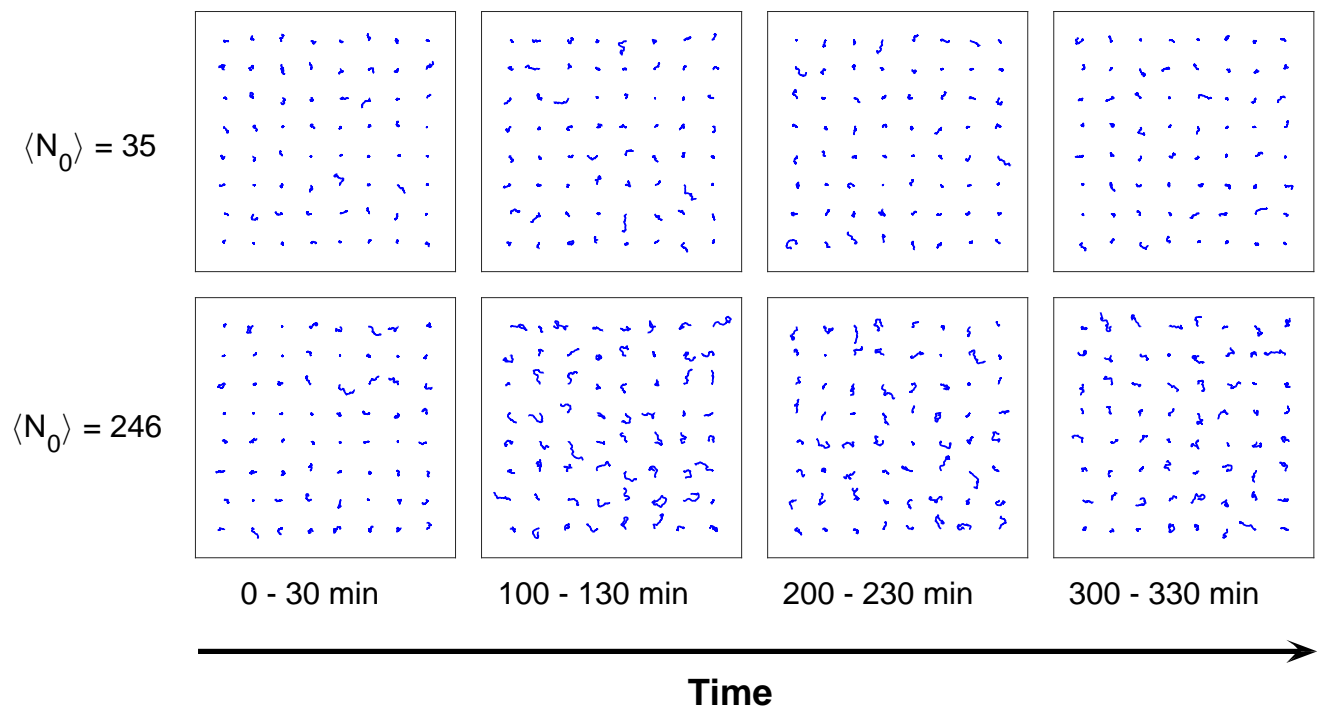


Supplementary Figure 3: Cells tend to be more elongated at high density.

Time evolution of the average eccentricity of the cell shapes' obtained by fitting ellipses for different initial densities $\langle N_0 \rangle$. The error bars are the standard deviations of the e distributions.

In *Dictyostelium discoideum*, the more persistent cells are also the more elongated ones, while the ones that exhibit rounded shapes usually move in a more random fashion^{11,52}. A way to measure the elongation of cells is to fit their shape with ellipses and compute the eccentricity $e = \sqrt{1 - \frac{b}{a}}$, where a and b are respectively the long and short axes of the ellipse. The eccentricity varies between 0 for a circle and 1 for an infinitely elongated ellipse. For instance, $e = 0.5$ corresponds to $a/b = 1.33$, $e = 0.7$ to $a/b = 1.96$ and $e = 0.9$ to $a/b = 5.26$. We measured the colony average of e as a function of time for different cell densities (Supplementary Figure 3). At early times, $\langle e \rangle$ goes up with cell density. It then relaxes to $\langle e \rangle \approx 0.55$ for all $\langle N_0 \rangle$. Although this elongation seems to be partly defined prior to the release of the stencil (see $\langle e \rangle$ at $t = 0$), a peak still appears in the densest condition, concomitantly with the peaks in $\langle v_r \rangle$ and ϕ_2 .

As for the persistence of cell trajectories, it increases transiently with no detectable pre-set dependence on density. To illustrate this fact, we show randomly sampled trajectories – all of the same 30 min duration – taken from experiments with low ($\langle N_0 \rangle = 35$) or high ($\langle N_0 \rangle = 246$) cell densities at different times (Supplementary Figure 4). At early times, most trajectories show a low persistence for both densities. This changes in the high density case where trajectories appear “unfolded” around $t = 100$ min, demonstrating the existence of runs with persistence time comparable to the 30 min path duration. At later times, the motion becomes again less persistent.



Supplementary Figure 4: Increase in single cell persistence.

Example of single cell trajectories from the lowest ($\langle N_0 \rangle = 35$) or highest ($\langle N_0 \rangle = 246$) cell density experiments, at times $t = 0 - 30$ min, $t = 100 - 130$ min, $t = 200 - 230$ min, $t = 300 - 330$ min. The persistence is seen to increase transiently around $t = 100$ min in the high density case, while at low density it does not change markedly in time. Grid spacing: $200 \mu\text{m}$.

3 Bimodal persistent motion

We found two modes in the decay of the velocity direction auto-correlation function (VDACF). As mentioned, either those two modes arise from two separate populations of cells, each having a single correlation time, or every single cell exhibit both modes. The first hypothesis is ruled out since it does not allow changes in the weights of the modes. In the second hypothesis, the motion of each cell follows a process with two characteristic times: this is the case of bimodal motion^{41,44,42}, but other models have this same property⁴³. Here we focus on the first option because it offers the simplest interpretation of a change in the weights c and c' in Equation (1). In the model proposed by Selmeczi *et al.*⁴³, it would mainly involve tuning their α parameter, which is the strength of a memory in a modified O.U. process: the underlying principle – regulation of the relative importance of two time-scales – is the same, but the formulation involves a higher degree of complexity which seems unnecessary here.

Model. We first characterise analytically a simple model of bimodal persistent motion. Assume a particle moves in the plane with velocity of constant magnitude v_0 . Its orientation is subject to rotational diffusion, but with a coefficient that alternates between two values D_{r1} and D_{r2} . The times spent in mode 1 and 2 are both exponentially distributed, with mean $\tau_1 = \lambda_1^{-1}$ and $\tau_2 = \lambda_2^{-1}$ respectively^a. What are the properties of such a random motion?

The essential quantity is the velocity direction autocorrelation function

$$C(t' - t) = \langle \mathbf{u}(t') \cdot \mathbf{u}(t) \rangle = \langle \cos [\theta(t') - \theta(t)] \rangle, \quad (5)$$

where $\mathbf{u} = (\cos \theta, \sin \theta)$ is the direction of motion. Let's introduce the probability densities $p_{i=1,2}(\theta, t)$ to be in mode i with orientation θ at time t , they are governed by

$$\partial_t p_1 = D_{r1} \partial_{\theta\theta}^2 p_1 + \lambda_2 p_2 - \lambda_1 p_1, \quad p_1(\theta, 0) = \phi_1 \delta(\theta), \quad (6a)$$

$$\partial_t p_2 = D_{r2} \partial_{\theta\theta}^2 p_2 - \lambda_2 p_2 + \lambda_1 p_1, \quad p_2(\theta, 0) = \phi_2 \delta(\theta), \quad (6b)$$

where $\phi_1 = \lambda_2 / (\lambda_1 + \lambda_2)$ (resp. $\phi_2 = \lambda_1 / (\lambda_1 + \lambda_2)$) is the fraction of time spent in mode 1 (resp. mode 2), and we have taken for initial orientation $\theta = 0$. Now, introducing $p(\theta, t) = p_1(\theta, t) + p_2(\theta, t)$, $C(t)$ can be expressed as

$$C(t) = \int_{-\pi}^{\pi} d\theta p(\theta, t) \cos \theta. \quad (7)$$

The system (6) can be solved using Laplace transforms for time and Fourier series for orientation, yielding

$$C(s) = \frac{(\lambda_1 + \lambda_2)^2 + \lambda_1(s + D_{r1}) + \lambda_2(s + D_{r2})}{(\lambda_1 + \lambda_2)[(s + D_{r1})(s + D_{r2}) + \lambda_1(s + D_{r2}) + \lambda_2(s + D_{r1})]},$$

where variable s is the Laplace variable. Going back to time domain, this expression translates into the sum of two exponentials

$$C(t) = c e^{-\gamma t} + c' e^{-\gamma' t}, \quad (8)$$

with the notations

$$\kappa^2 = (D_{r1} + D_{r2} + \lambda_1 + \lambda_2)^2 - 4(D_{r1}D_{r2} + D_{r1}\lambda_2 + D_{r2}\lambda_1), \quad (9a)$$

$$\kappa'^2 = (D_{r1} - D_{r2} + \lambda_1 - \lambda_2)^2 + 4\lambda_1\lambda_2, \quad (9b)$$

$$\gamma = (\kappa + D_{r1} + D_{r2} + \lambda_1 + \lambda_2)/2, \quad (9c)$$

$$\gamma' = \gamma - \kappa, \quad (9d)$$

$$c = 1 - c' = -\frac{(D_{r1} - D_{r2})(\lambda_1 - \lambda_2) + (\lambda_1 + \lambda_2)(\lambda_1 + \lambda_2 - \kappa')}{2\kappa(\lambda_1 + \lambda_2)}. \quad (9e)$$

^aThe value of D_r is thus a Telegraph process.

It can be shown that the following inequalities hold

$$c, c' \geq 0, \quad D_{r2} \leq \gamma' \leq D_{r1} < \gamma, \quad (10)$$

showing that both terms are always decaying, and that the slowest relaxation is intermediate between D_{r1} and D_{r2} .

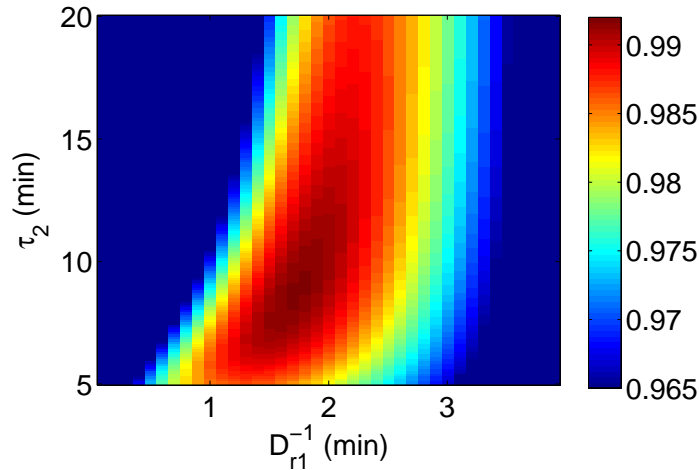
In the limit $D_{r1} \rightarrow \infty$, *i.e.* when all directional persistence is lost in mode 1, all expressions greatly simplify

$$\gamma = D_{r1}, \quad \gamma' = D_{r2} + \lambda_2, \quad c' = \frac{\lambda_1}{\lambda_1 + \lambda_2}, \quad (11)$$

where only the first term in the expansion has been retained. In this case, $C(t)$ exhibits a rapid drop with characteristic time $\sim D_{r1}^{-1}$, followed by a slowest decay whose constant $\gamma' = D_{r2} + \lambda_2$ is independent of D_{r1} and whose prefactor c' is the fraction of time spent in mode 2. On further assuming that mode 2 involves ballistic motion ($D_{r2} = 0$), then $\gamma' = \lambda_2$, giving access to the mean duration of mode 2. In this particular case, the relationship between the biexponential form of correlation function and the model parameters is simple. This is not so, however, in the general case, and accordingly we have resorted to a fitting procedure.

Fitting procedure – experimental data.

We use the expressions above (8 & 9) to fit all experimental correlation functions. Since mode 2 is assumed ballistic, $D_{r2} = 0$. The parameters D_{r1} and τ_2 , considered as intrinsic properties of the cells, are common to all curves and are thus heavily constrained. The free parameters remaining for each curve are τ_1 , and an additional constant prefactor that allows $C(t = 0)$ to differ from unity. In practice, we first varied systematically the values of D_{r1} and τ_2 . For each couple, we fitted the complete set of 15 $C(t)$ curves (5 first time-windows for each of the 3 density conditions) with the two mentioned free parameters. We used the value of R^2 averaged on these 15 curves to estimate the quality of the fit for a given couple (D_{r1}, τ_2). This yielded unambiguously the optimal values $D_{r1}^{-1} = 1.7$ min and $\tau_2 = 8.6$ min (Supplementary Figure 5). Then we measured τ_1 by fitting again all the curves using these optimised fixed parameters.

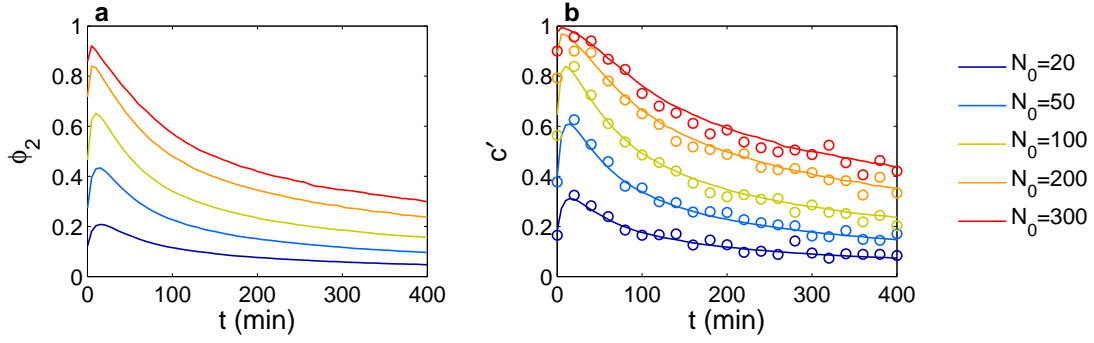


Supplementary Figure 5: Parameter space for the fitting procedure.

The average R^2 computed from 25 experimental curves of correlation functions exhibits a clear peak at $D_{r1}^{-1} = 1.7$ min and $\tau_2 = 8.6$ min. Here, the time-windows for $t \geq 200$ min were not considered in order not to overweight the long-term behaviours. Using the complete set of 39 curves slightly moves the peak of R^2 but then $D_{r1}^{-1} = 2$ min and $\tau_2 = 10$ min remain excellent estimates.

In using the model, we have tacitly assumed that at each time, the population of cells is “equilibrated” between the two modes. This is reasonable since the residence time in each mode (τ_1 and

$\tau_2 = 10$ min) remains smaller than the time scale over which λ_1 (or the density) significantly varies (around 100 min).



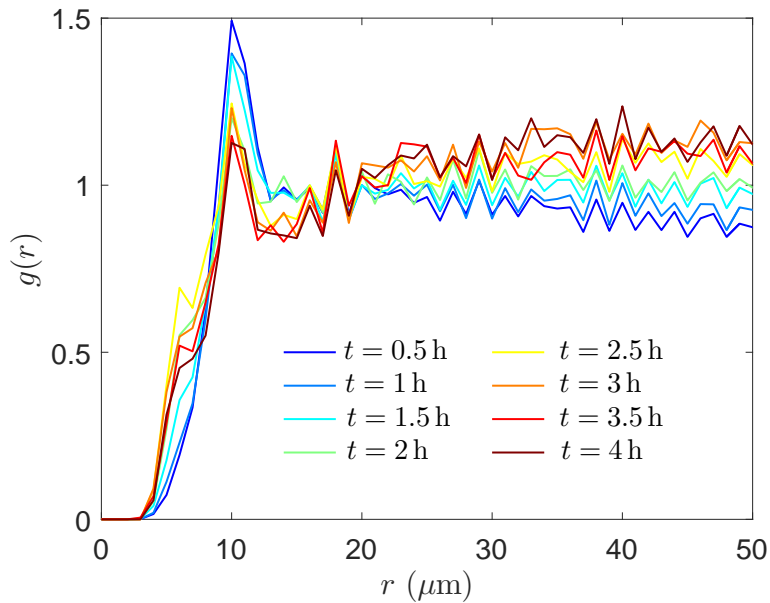
Supplementary Figure 6: Simulations – Results of the fitting of the velocity autocorrelation functions applied to simulations with CEL.

(a) Proportion of cells in mode 2. (b) Prefactor c' of the longest relaxation in the correlation function. Theoretical prediction from ϕ_2 (—) and measurement from the correlation functions (o).

Fitting - simulations with CEL. We computed the proportion of particles in persistent mode ϕ_2 at all times (direct output from the simulations, Supplementary Figure 6a) and the velocity autocorrelation functions at various times and for all particle numbers N_0 . From the latter, we could extract the parameters from a fit with expression (8). In particular we compared the obtained c' values to the theoretical predictions (9e) (Supplementary Figure 6b). They are in close agreement with each other, showing that the hypothesis of equilibration between the two modes through λ_1 , under the control of collisions, is reasonable.

4 Analysis of pair collisions

4.1 Detection of contacts.



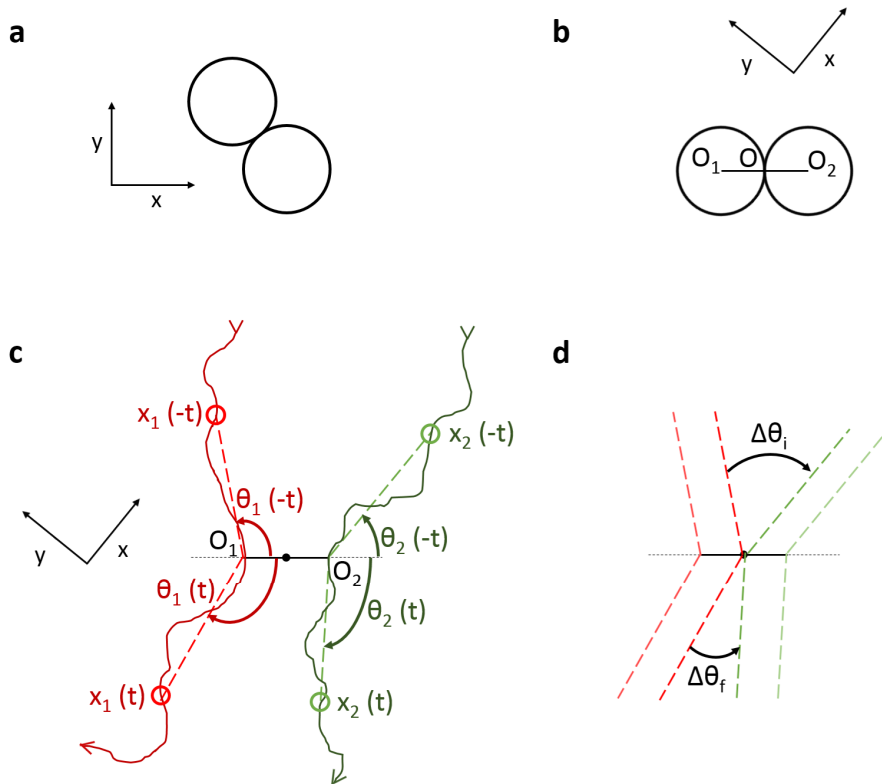
Supplementary Figure 7: Radial distribution function, averaged over all the experiments, at various time points.

We study here the effect of cell-cell contacts on the trajectories. To that end, we need to find a way to disentangle this effect from other biases related to the occurrence of contacts: For instance, contacts are more likely to happen in dense areas, where the behaviour is known to be different on average from sparser zones. For that reason, and to avoid increasing the number of spurious underlying parameters, we only focused on two-body interactions.

A cell-cell contact was defined by two cell positions being closer than a distance d_{max} . If the cells remain close longer than one time frame, the collision time t_0 is defined as the time at which the cell-cell distance is minimal. Moreover, since our measurements cannot be instantaneous – *ie* they are based on pieces of trajectories extending over several time frames – we selected only those collisions involving two cells that did not encounter any other collision for a time t_{free} before and after t_0 , hence reducing drastically the number of exploitable data.

Contrary to the simulations, for which the interaction radius is well-defined, the choice of d_{max} is not trivial in experiments because cell shapes and sizes are distributed. Thus, to fix d_{max} we first measured the radial distribution function $g(r)$ (Supp. Fig. 7). The profiles, computed at different times, all show a marked peak at $r = 10 \mu\text{m}$. As a consequence, we chose a slightly larger $d_{max} = 11 \mu\text{m}$ to detect reliably the contacts between cells.

4.2 Angular deflection

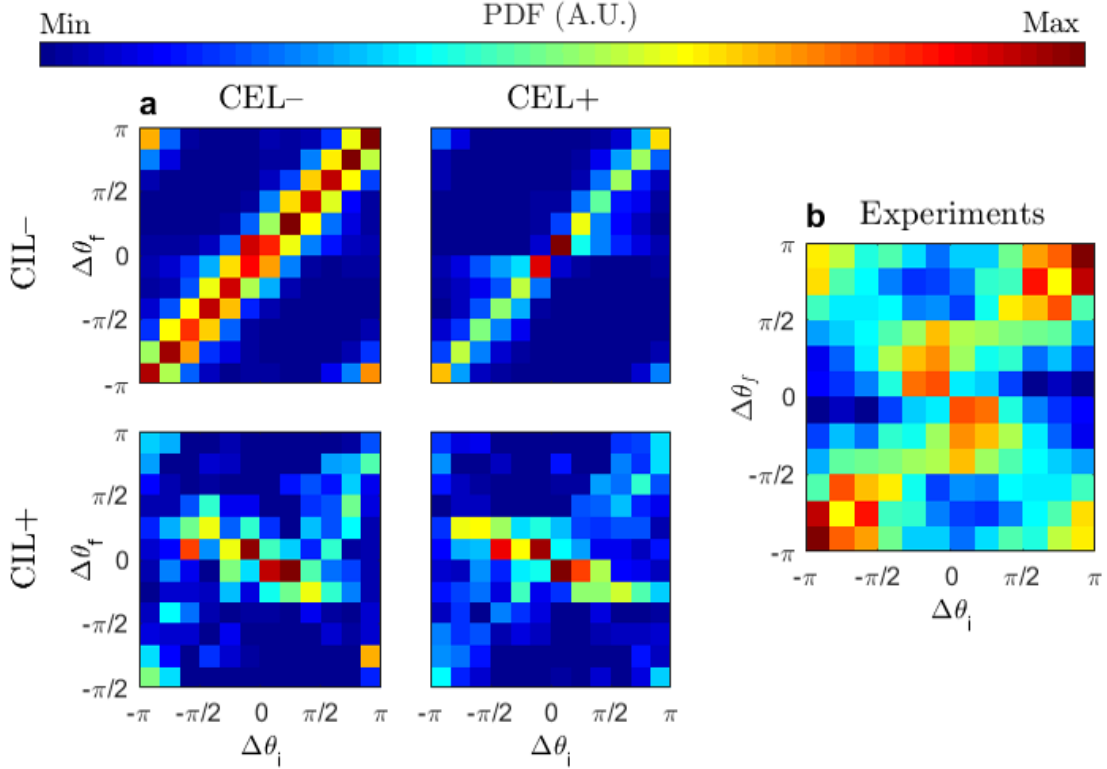


Supplementary Figure 8: Sketch of the angle definition.

(a) A cell-cell contact is detected in the frame of the picture. (b) The frame is rotated so that the (O_1OO_2) axis becomes the new x-axis, where O_i is the position of cell i and O is the barycentre of the collision. (c) The incidence (resp. scattering) angle $\theta_{1/2}(-t)$ (resp. $\theta_{1/2}(t)$) is measured from the cell's position at $-t$ respective to its position at the time of the contact. (d) The incidence (resp. scattering) angle separation $\Delta\theta_i$ (resp. $\Delta\theta_f$) is the difference between the two directions of motion of the cell couple.

We studied in details the statistics of incidence and scattering angles, both in simulations and experiments. To that end, we detected the collisions with $t_{free} = 3 \text{ min}$ before and after the collision.

As depicted in Fig. 8 the cell coordinates were rotated so that the (O_1O_2) axis is the new x -axis, where O_1 and O_2 are the positions of cell 1 and 2 at collision time, and O is the center of $[O_1O_2]$. We then measured the mean angles of motion $\theta_i(\pm t)$, where $i \in \{1, 2\}$ and $t \in \{1, 2, 3\}$ min, defined as the angle between $(O_iX_i(t))$ and (OO_i) and computed $\Delta\theta_i = \theta_2(-t) - \theta_1(-t)$ and $\Delta\theta_f = \theta_2(t) - \theta_1(t)$, the incidence and scattering angles respectively. Trying to decipher the effect of the collision, we are especially interested in the relative scattering $\Delta\theta_f$ as a function of $\Delta\theta_i$. In Fig. 9, we show the heat maps for the probability densities $\mathbb{P}(\Delta\theta_f|\Delta\theta_i)$.



Supplementary Figure 9: Angular deflection at collision in simulations and experiments.

$\mathbb{P}(\Delta\theta_f|\Delta\theta_i)$ for collisions detected with $d_{max} = 11.2 \mu\text{m}$, $t_{free} = 3$ min, at $t_{f/i} = \pm 1$ min. (a) Simulations without (CIL-) or with (CIL+) repulsive torque and monomodal ($D_r^{-1} = 10$ min, CEL-) or bimodal (CEL+) motion. (b) Experimental data gathered from all experiments.

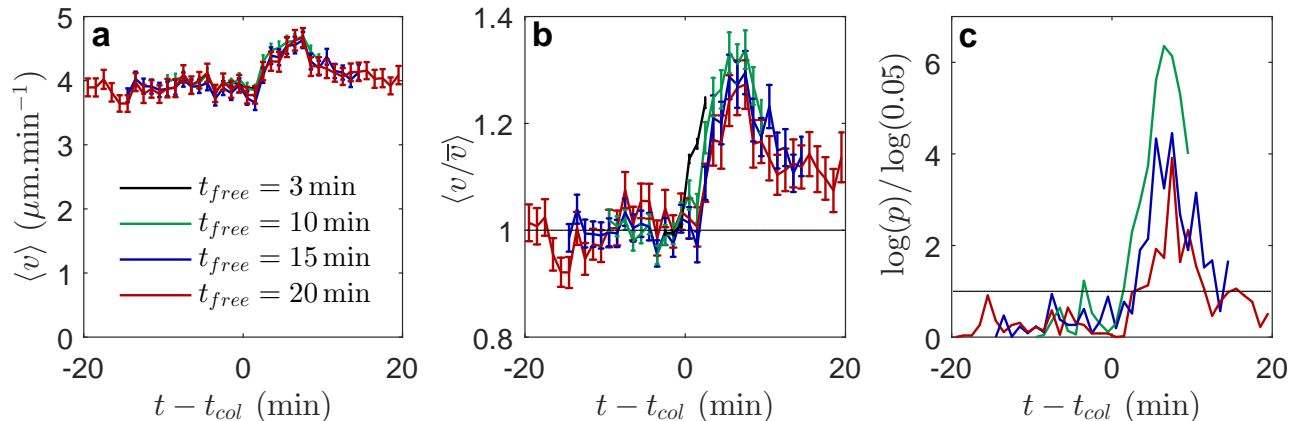
In simulations without CIL, the probability distribution $\mathbb{P}(\Delta\theta_f|\Delta\theta_i)$ is concentrated around the main diagonal $\Delta\theta_f = \Delta\theta_i$. It means that the relative direction of motion remains unaffected by the collision, hence that the particles cross “without seeing” each other (in terms of direction of motion). It is consistent with the simulation rule that the interaction only involves a pushing force during the contact, but the intrinsic direction of motion is not modified.

The results are completely different in simulations with CIL (introduced in the form of a repulsive torque). Most of the probability concentrates in a zone where $\Delta\theta_i$ and $\Delta\theta_f$ have opposite signs, a signature of the angular repulsion.

In the experimental data, two distinct behaviors seem to be present: There is both a concentration of probability around both diagonals, $\Delta\theta_f = \Delta\theta_i$ denoting crossing, and $\Delta\theta_f = -\Delta\theta_i$, a signature of specular reflection. In particular, $\Delta\theta_f = -\Delta\theta_i$ seems more likely for small $\Delta\theta_i$, when the incident trajectories are close to being parallel, while $\Delta\theta_f = \Delta\theta_i$ is predominant near $\|\Delta\theta_i\| = \pi$. These results support the idea that even in the event of a collision, *Dictyostelium discoideum* cells reorient smoothly so as to bypass their encounter: at low incidence angle crossing is difficult while almost specular reflection demands only a slight turn, and at higher incidence it is easier to circumvent each other. It is different from the usual view of CIL, according to which colliding cells reorient specifically away along the contact axis. It could be related to the increased probability for D .

discoideum cells to form new pseudopods in the protruded area rather than along the cell body³⁷, acting together with a CIL-like inhibition of protrusions in the cell-cell contact zone. In any case, they show that the cell-cell contacts have no aligning effect on the direction of motion, and thus could not generate a coherent motion that would be responsible for the increase of the colony spreading rate

4.3 Contact enhancement of locomotion.



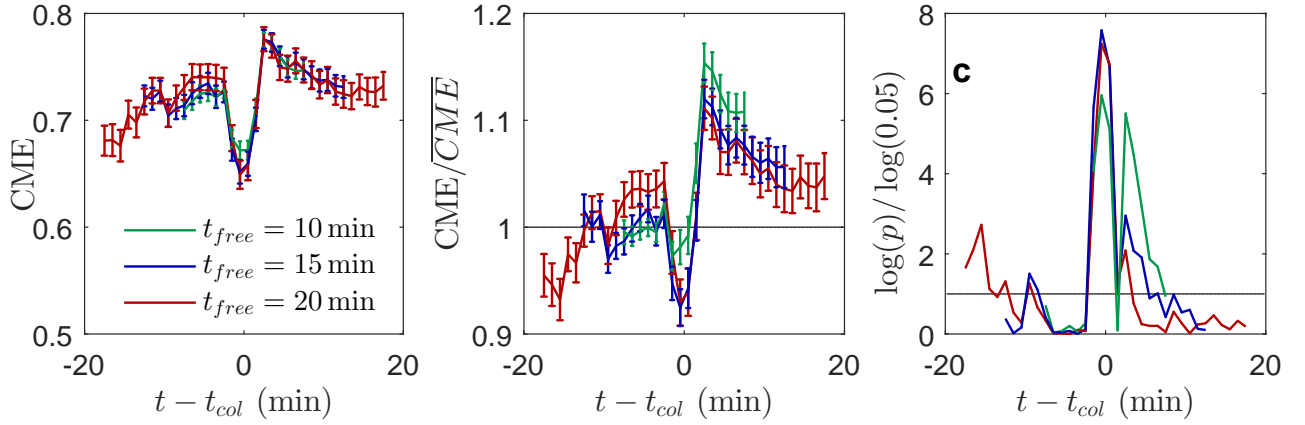
Supplementary Figure 10: Increase in cell speed after collisions.

(a) Average speed before and after a single collision, using smoothed trajectories with $\delta t = 1$ min and $t_{free} = 3$ (black), 10 (green), 15 (blue) and 20 min (red). Mean \pm SEM for $n = 6578, 376, 232$ and 153 cell pairs respectively. (b) Average normalised speed v/\bar{v} , where \bar{v} is the basal speed of a single cell before and after collisions. Same δt , t_{free} and number of contacts as in (a). (c) Logarithm of the p -value obtained from the Kolmogorov-Smirnov test against the null hypothesis that $v(t)/\bar{v}$ is distributed with the same PDF as $v(-t_{free})/\bar{v}$. Values above 1 denote when the null hypothesis can be rejected with more than 95% confidence.

Cell speed. Similarly as for the direction of motion, we measured the instantaneous speed of cells undergoing a single collision in a frame with free motion t_{free} before and after the collision. We found that on average, the cells exhibit a transient increase of their speed after collisions. Because of positional noise, this effect is not completely clear using the experimental time frame $\delta t = 20$ s. Yet it is better seen after smoothing the trajectories over $\delta t = 1$ min, and varying t_{free} from 3 min to 20 min: $t_{free} = 20$ min provides a view of the long-term dynamics; with shorter t_{free} , the complete time-frame is not accessible, but the trend for $\langle v \rangle(t)$ is confirmed with much more statistics (up to 6578 cell-cell contacts measured with $t_{free} = 3$ min).

The cells accelerate for 7 – 8 min following collisions, reaching an average speed approximately 20% higher than the “basal” average speed, and then the speed decreases back to its basal value at a similar rate. When the speed of each single cell is normalised by its own basal speed \bar{v} (*i.e.* its mean speed prior to the collision), one even gets a 30% increase on average. Although these changes are relatively small compared to the standard deviation of the speed distribution in the cell population, a statistical analysis using the Kolmogorov-Smirnov test shows that the distribution differs significantly from the distribution at $t = -t_{free}$ only for ~ 12 min after collisions.

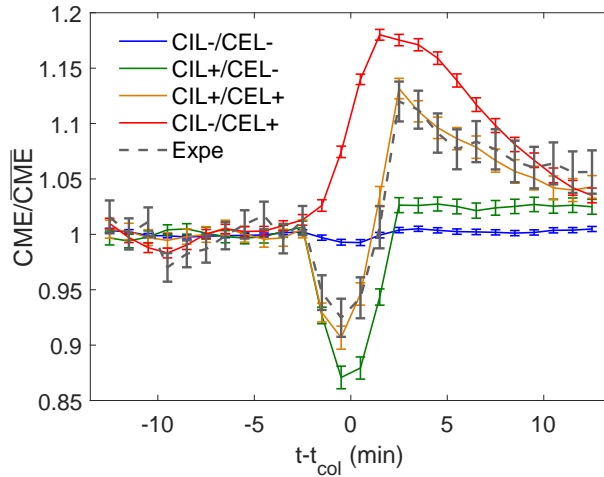
Persistence time. Using again smoothed trajectories with $\delta t = 1$ min to make the patterns of evolution more apparent, we repeat the analysis on the CME computed for $\Delta t = 5$ min (see Methods). This revealed a CME drop around the contacts, as well as a subsequent transient increase (Supp. Fig. 11a-b). Both effects seemingly arise from significant changes in the distribution of the



Supplementary Figure 11: Increase in CME after collisions.

(a) Average CME before and after a single collision, using smoothed trajectories with $\delta t = 1$ min and $t_{free} = 10$ (green), 15 (blue) and 20 min (red). Mean \pm SEM for $n = 376, 232$ and 153 cell pairs respectively. (b) Average normalised CME \overline{CME}/CME , where \bar{v} is the basal speed of a single cell, before and after collisions. Same δt , t_{free} and number of contacts as in (a). (c) Logarithm of the p -value obtained from the Kolmogorov-Smirnov test against the null hypothesis that $CME(t)$ is distributed with the same PDF as $CME(-t_{free})$. Values above 1 denote when the null hypothesis can be rejected with more than 95% confidence.

CME (Supp. Fig. 11c). The depression is probably related to changes in direction during the contact. The increase, between 10 and 15% for single cells on average, shows that the persistence of the motion is enhanced for at least a few minutes after a cell-cell contact.



Supplementary Figure 12: Single-cell-normalised CME: comparison of various simulation conditions with experimental data. Mean \pm SEM, $t_{free} = 15$ min.

Sensitivity of CME measurements to the presence of CEL. While in the case of the speed the measurement is direct, the CME is only a proxy to estimate whether the trajectories are more or less persistent on a given time-scale Δt . As a consequence, we also tested our CME-based analysis of collisions on the simulation data. It makes apparent that a drop in CME around 10% is the signature of CIL (in the sense of turning upon contact), while a transient increase in CME of 10–20% is observed only in the presence of CEL (Supp. Fig. 12).

Finally, the experimental curve aligns closely with that of the CIL+/CEL+ simulations (Supp. Fig. 12). Without proving that the cells follow the precise rules implemented in the simulations, it

shows that CIL and CEL seem to be necessary to account for the experimental collision data.

Supplementary movies

Supplementary movie 1 Long-time spreading of a colony with high cell density.

Supplementary movie 2 Short-time (200 min) dynamics of a colony with low cell density. $N_0 = 18$.

Supplementary movie 3 Short-time (200 min) dynamics of a colony with high cell density. $N_0 \simeq 275$.

Supplementary movie 4 Simulation of active particles at low density undergoing CEL. $N_0 = 20$.

Supplementary movie 5 Simulation of active particles at high density undergoing CEL. $N_0 = 200$.